Available online at www.sciencedirect.com
ScienceDirect
Journal of Computational Physics 227 (2008) 6754–6778
JOURNAL OF COMPUTATIONAL PHYSICS
www.elsevier.com/locate/jcp

CFD-based application of the Nyquist criterion to thermo-acoustic instabilities

J. Kopitz, W. Polifke *

Lehrstuhl für Thermodynamik, Technische Universität München, D-85747 Garching, Germany

Received 23 April 2007; received in revised form 31 January 2008; accepted 18 March 2008
Available online 28 March 2008

Abstract

A novel approach for the analysis of self-excited instabilities in thermo-acoustic systems is proposed. Combining computational fluid dynamics with low-order acoustic modeling, the open-loop transfer function of the system under investigation is computed. The system eigenmodes and the linear stability characteristics are then deduced from a Nyquist plot.

The method is suitable for systems where – due to geometrical complexities or non-compact regions of heat release – a low-order formulation is not appropriate or not available. Explicit knowledge of the frequency response or the transfer matrix of the heat source is not required. Further advantages of the new approach are discussed in the paper.

To establish proof of concept, the method is validated against a simple model of a Rijke tube. Over the frequency range considered, frequencies and growth rates of stable as well as unstable eigenmodes are predicted accurately. The new method, combining flow simulation, low-order acoustic modeling and control theory, makes possible a comprehensive analysis of acoustic stability behavior of complex thermo-acoustic systems at comparatively modest computational cost.

PACS: 02.30.Yy; 43.28.Kt; 43.35.Ud; 43.60.Bf; 47.50.Gj; 52.35.Dm

Keywords: Thermo-acoustics; Instabilities; Computational fluid dynamics; Control theory

1. Introduction

Research on self-excited thermo-acoustic instabilities, a phenomenon arising primarily from the interaction of acoustic waves and unsteady heat release in a compressible fluid, has a long and multifaceted history [1–4]. In combustion applications, thermo-acoustic instabilities are in general an undesirable phenomenon and can lead to excessive emissions of noise and pollutants or even structural damage [5–10].

It is the goal of ongoing research to identify instability mechanisms, determine stability limits and evaluate the effectiveness of counter measures in early design stages of a combustor. Unfortunately, the experimental investigation of combustion instabilities in scaled-down test rigs delivers often at considerable cost only very

* Corresponding author. Tel.: +49 89 28916216; fax: +49 89 28916218.
E-mail addresses: Kopitz@gmx.net (J. Kopitz), Wolfgang.Polifke@tum.de (W. Polifke).

0021-9991/$ - see front matter © 2008 Elsevier Inc. All rights reserved.
doi:10.1016/j.jcp.2008.03.022

limited insight. Consequently, various methods for semi-analytical or numerical analysis of thermo-acoustic systems have been developed.

For example, with computational fluid dynamics (CFD) it is possible to simulate the temporal development of low-amplitude, random perturbations imposed on a steady solution of the flow equations. If the system considered is linearly unstable, perturbation amplitudes will grow with time and develop into an oscillatory mode with distinct frequency, eventually evolving into a limit cycle. In this way one can assess the thermo-acoustic stability of a combustor, even without explicit knowledge of the frequency response of the flame or the transfer matrix of the burner [11–13]. However, there are significant problems with the formulation of appropriate boundary conditions, which should provide a consistent formulation for the mean flow, give the correct acoustic impedance and in addition be numerically robust [14,15]. A further drawback is that with this approach only the dominant unstable mode is found. Unstable modes with smaller growth rates or stable modes cannot be identified. Finally, the required compute resources are immense, especially for practical geometries.

To circumvent these difficulties, various hybrid methods for the analysis of thermo-acoustic instabilities have been developed in recent years, which follow a strategy of "divide and conquer": efficient models for the system acoustics are combined with a parametrized, low-order description of the response of the heat release rate to flow perturbations. Typically, the latter is formulated in terms of the frequency response or the transfer matrix of the heat source of the system, obtained from experiment or computational fluid dynamics.

The following approaches can be distinguished:

- Low-order models or "network models" are popular because they are fast and flexible and provide physical insight [6,8,16–18]. However, the applicability to complicated geometries or distributed regions of heat release is limited.
- Finite element or finite volume formulations for the wave equation – or, more generally speaking, acoustic perturbation equations – do not suffer from that shortcoming [19–21]. On the other hand, compute requirements are higher, the implementation of acoustic boundary conditions can be difficult, and it may not be possible to take into account mean flow effects.
- Galerkin or state–space techniques, which rely on expansion of the acoustic field in terms of a set of basis functions, share some of the advantages as well as disadvantages with alternative approaches [22–24].

It is emphasized that all these methods do not compute the response of the flame (in general: the heat source) to perturbations of the flow. Instead, information about the flame dynamics is required *input* for these models, and is typically provided in terms of the frequency response of the flame. The frequency response is in simplest terms defined as the normalized response of the overall heat release rate $\dot{Q}$ of the flame to a perturbation of the flow velocity u_c at a reference location upstream of the flame (typically at the burner mouth, say):

$$F(\omega) \equiv \frac{\hat{\dot{Q}}/\bar{\dot{Q}}}{\hat{u}_c/\bar{u}_c}. \tag{1}$$

However, for combustor configurations of practical interest, a frequency response as defined in the above equation does not always provide an appropriate characterization of the flame dynamics. Firstly, it has been pointed out that the reference location should be chosen with care, otherwise the transfer function as defined above does not provide a description of flame dynamics that is independent of the combustor impedance [25]. Secondly, for acoustically non-compact flames (spatial extent of the region of heat release is comparable to relevant acoustic wave lengths), a local response $F(\omega,\vec{x})$ should be used [21,26–28] instead of a global frequency response $F(\omega)$. Furthermore, if the fuel injector is not acoustically decoupled from the combustion chamber, a premix flame can in general not be represented as a single-input/single-output element and an extended description must be developed. For example, it has been suggested to employ a multiple-input/single-output flame transfer function, or instead the acoustic transfer matrix of burner and flame [29–33].

The accurate and efficient determination of flame transfer functions or burner transfer matrices by analytical methods, experiment or computation is a challenging task and the topic of several ongoing research projects [21,28,33–39].

In this paper, an alternative method for stability analysis is proposed, which does not require explicit knowledge of the frequency response of the heat source (and indeed does not make a priori assumptions about the input/output structure of the flame dynamics model): An unsteady flow simulation with broad-band external excitation is linked to a network model in order to compute the open-loop transfer function (OLTF) of the thermo-acoustic system. The stability characteristics of the system are then deduced from the OLTF with graphical methods familiar from control theory, i.e. interpretation of the Nyquist plot [40–44]. As the proposed method integrates computational fluid dynamics, network modeling and the stability criterion of Nyquist, it shall be referred to as the "CNN"-approach in the following.

The motivation of the present paper is to introduce the new approach and to establish proof of concept for the method. First, the Nyquist stability criterion and its adaptation to thermo-acoustic stability analysis [42–44] are reviewed. Readers who are familiar with the Nyquist criterion, as it is taught in every course on control theory, may skip the next sub-section and continue reading in Section 2.2, where the application of the Nyquist criterion to thermo-acoustic systems is discussed. Then it is described, how computational fluid dynamics and low-order network modeling are combined to determine the OLTF of the thermo-acoustic system. Results of a validation study are presented in the following section, based on a simple model of a Rijke tube. This is a "classical" thermo-acoustic system which has been investigated as early as 1859 [1,45,46]. For this simple system, semi-analytical results obtained with a network model may be considered as an exact reference solution.

Further possible areas of application, which go beyond this simple system, and expected benefits of the CNN approach are discussed briefly. Validation against numerical or experimental results for more realistic configurations including combustion is the subject of ongoing work and shall be presented elsewhere.

2. The Nyquist stability criterion

The Nyquist stability criterion is a well-known tool in control theory. It allows to test for stability of a closed-loop system by inspection of the "Nyquist plot" of the open-loop transfer function (OLTF) [41]. In this section, a brief review of the method is given, then the application to a thermo-acoustic system is discussed.

2.1. Review of stability analysis with Nyquist plots in control theory

Consider a system as shown in Fig. 1 with open-loop transfer function $G(s)$ and unit negative feedback $H(s) = 1$, such that

$$x_1 = G(s)(x_0 - x_1), \tag{2}$$

and therefore

$$x_1 = \frac{G(s)}{G(s)+1} x_0. \tag{3}$$

The characteristic equation, from which stability can be deduced, is then

$$G(s) + 1 = 0. \tag{4}$$

The system is stable, if all the roots s_n of this equation are located in the left half of the complex plane. In that case, all perturbations of the system will decay exponentially $\sim e^{st}$ with time.

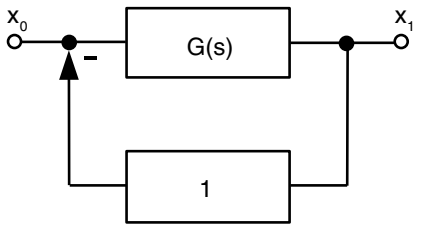

Fig. 1. Open-loop system with unit negative feedback.

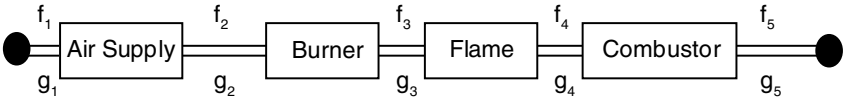

Fig. 2. Network model of a combustion system comprised of air supply ("plenum"), burner, flame and combustor. The unknowns of the model are the characteristic wave amplitudes f_i and g_i at the "nodes" of the network. Boundary conditions can be expressed as reflection coefficients $r_i(\omega) = \hat{f}_1/\hat{g}_1$ at the inlet and $r_o(\omega) = \hat{g}_5/\hat{f}_5$ at the outlet, respectively.

To locate all the roots can be tedious, therefore alternative methods to assess the stability have been developed. For example, in control theory the transfer function is usually a fraction of polynomials

$$G(s) = \frac{P_N(s)}{P_D(s)} = \frac{a_n s^n + \cdots + a_0}{b_m s^m + \cdots + b_0}. \tag{5}$$

The *Routh–Hurwitz* stability criterion exploits this fact and allows to determine system stability from the polynomial coefficients [41].

Alternatively, one can deduce stability from the *Nyquist plot*, i.e. a polar plot of the imaginary axis[1] mapped through the open-loop transfer function. The associated Nyquist stability criterion is based on Cauchy's argument principle, which states the following: *Consider an analytical function $f(z)$ with a number Z of zeros $f(z) = 0$ and a number P of poles $f(z) \to \infty$ within a simple closed contour C in the complex plane. Then the winding number of the image curve of the contour C mapped $f(z)$ around the origin $0 + i0$ is equal to $Z - P$.*

For the characteristic equation (4) and the Nyquist plot, Cauchy's argument principle implies that the number Z of zeros of the OLTF $G(s)$ in the right half of the complex plane is related to the number N of positive encirclements (i.e. in clockwise direction) of the "critical point" -1 and the number of poles P of $G(s)$ as follows:

$$N = Z - P. \tag{6}$$

For a stable system, no roots of the characteristic equation (4) should be on the right side of the s-plane, i.e. $Z = 0$. Nyquist's criterion follows with Eq. (6): *for stability, the number N of anticlockwise encirclements about the critical point -1 must be equal to P, the number of open-loop poles in the right half plane.*

2.2. Application of the Nyquist criterion to thermo-acoustic systems

It is by no means obvious how the Nyquist criterion can be employed to analyse the stability of thermo-acoustic systems. In this section, the network-model-based approach for generation of a Nyquist plot proposed by Polifke et al. is reviewed [42,43].

A linear network-model as sketched in Fig. 2 comprises a number of two-ports, each of them representing a discrete element of the system. Mathematically, each two-port is described by a transfer matrix, with the matrix coefficients linking the acoustic variables $(p'/\varrho c, u')$ – or equivalently the characteristic wave amplitudes (f, g), see Section 5 for definitions – at the ports of the element. This formulation, complete with appropriate boundary conditions at the terminations of the network, results in a homogeneous system of equations

$$\mathbf{S}\vec{x} = 0 \tag{7}$$

with the vector of unknowns $\vec{x} = (\hat{f}_1, \hat{g}_1, \ldots, \hat{g}_N)$, see [6–8,16,43] for details and examples. Solutions of the system, i.e. eigenmodes with frequency ω_n, are found by computing the roots of the characteristic equation $\mathrm{Det}(\mathbf{S}) = 0$.

The eigenfrequencies are in general complex-valued, the imaginary part of the eigenfrequencies determines stability: With time dependence $\sim \mathrm{e}^{\mathrm{i}\omega t}$, a positive imaginary part $\Im(\omega_n)$ corresponds to exponential decay of

[1] Strictly speaking, the Nyquist plot is the image of the Nyquist contour, which is a closed contour encompassing the right half of the complex plane. Starting from $-i\infty$ one moves along the imaginary towards $+i\infty$ and then in a clockwise circular arc with radius $r \to \infty$ back to the point $-i\infty$.

Fig. 3. Diagnostic dummy.

the nth eigenmode, i.e. stability, and vice versa for an unstable eigenmode. A growth rate or *cycle increment* of mode n can be derived from the eigenfrequency:

$$\Gamma \equiv \exp\left\{-2\pi \frac{\Im(\omega)}{\Re(\omega)}\right\} - 1. \tag{8}$$

The growth rate indicates by which amplitude ratio a mode increases or decreases per cycle. For example, a growth rate of $\Gamma = 0.2$ indicates an increment of the amplitude of 20% per cycle.

To establish an analogy to control systems and to define the equivalent to the open-loop transfer function, the network model must be "cut open". Polifke et al. have shown how this can be done for networks of arbitrary topology by introducing a "diagnostic dummy" element in the network [42,43]. As indicated in Fig. 3, two of the four variables are simply linked across the two-port, e.g. $\hat{g}_d = \hat{g}_u$, while the second pair of variables is not connected. Note that by inserting the diagnostic dummy, the homogeneous system of Eqs. (7) changes into an inhomogeneous system $\mathbf{S}'\vec{x}' = b$ with r.h.s. $b = (0, \ldots, 1, \ldots, 0)$. Now one can define the OLTF of the thermo-acoustic system with diagnostic dummy as

$$G(\omega) = -\frac{\hat{f}_u}{\hat{f}_d}. \tag{9}$$

The minus sign is introduced to maintain close analogy with negative feedback control systems.

In general, i.e. for arbitrary frequency ω, the solution $\vec{x}'(\omega)$ of the inhomogeneous system with diagnostic dummy will not be equal to any of the eigenmodes of the original system Eq. (7). In this case the values of the unconnected variables across the diagnostic dummy will not be equal, i.e. $\hat{f}_d \neq \hat{f}_u$. However, for every eigenfrequency ω_n, the solutions $\vec{x}'(\omega_n)$ of the system with diagnostic dummy will be identical to the corresponding eigenvector $\vec{x}_n$ of the original system (up to an arbitrary scaling factor), and the acoustic variables will match across the "cut", $\hat{f}_d = \hat{f}_u$. It follows that Eq. (9) defines a mapping, which maps every eigenmode of the homogeneous system Eq. (7) to the critical point -1, i.e. $G(\omega_n) = -1$ for every eigenfrequency ω_n. This important property of the OLTF will be exploited in the following.

Although the equivalent to the open-loop transfer function is now defined, the classical Nyquist criterion, as it was formulated in the previous section, is not directly applicable to a thermo-acoustic system: As already mentioned, low-order models for thermo-acoustic stability analysis are commonly formulated with harmonic time dependence $\sim e^{i\omega t}$, and the imaginary part of the angular frequency ω determines stability. For a stable system, no eigenfrequencies ω_n must be located in the lower half of the complex plane. This implies for the Nyquist plot, that the real axis of the ω-plane is mapped by the open-loop transfer function to the $G(\omega)$-plane.

Once these modifications are taken into account, one could in principle proceed with application of the criterion in complete analogy to control theory. However, transfer functions in thermo-acoustics are in general not polynomials in ω or fractions thereof, but involve harmonic or exponential functions.[2] The identification of poles is in this case no easier than the determination of eigenfrequencies by iterative numerical solution of the characteristic Eq. (4). Moreover, the coefficients of acoustic transfer matrices – the building blocks of network models – are not always given in analytical form. In this case, the OLTF cannot be evaluated for complex-valued frequencies with imaginary part $\Im(\omega) \neq 0$. These difficulties are also discussed in [42,43].

Therefore, a modified rule for the interpretation of Nyquist plots has been put forward, which is more suitable for application to thermo-acoustic systems [42,43]. The proposed rule is based on a property of analytical functions: An analytic function is *conformal*, i.e. it preserves local angles or "handedness", at any point where

[2] Incidentally, for this reason application of the Routh–Hurwitz criterion to thermo-acoustic systems is not possible.

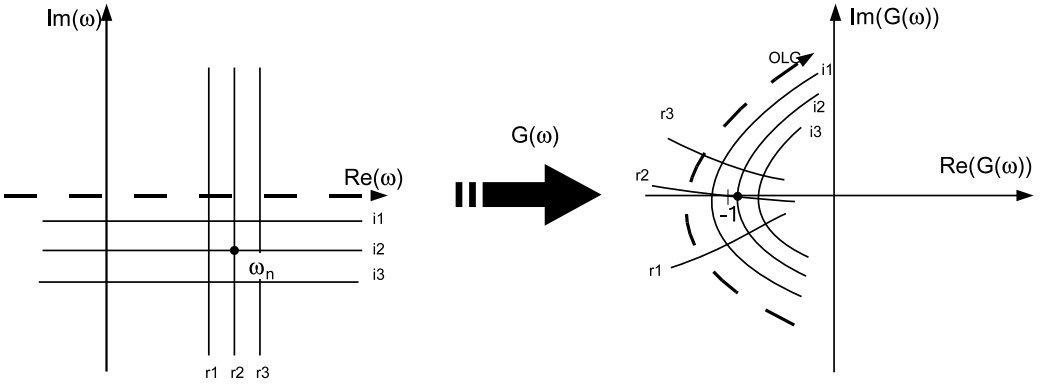

Fig. 4. Conformal mapping $\omega \to G(\omega)$ of the real axis under the OLTF for an unstable eigenfrequency.

it has a non-zero derivative [47]. Consider now the open-loop transfer function $G(\omega)$ as a conformal mapping from the ω-plane onto the G-plane, see Fig. 4. The real axis $\Im(\omega) = 0$ in the ω-plane (left graph) and its image in the G-plane (right graph) are indicated by the thick dashed line with arrow head. According to Eq. (9), the eigenfrequencies (roots of the characteristic Eq. (4)) ω_n are mapped to the critical point -1. Because the conformal mapping $\omega \to G(\omega)$ preserves handedness, the -1 point will lie to the left (right) of the image curve of the real axis if the corresponding root ω_n lies in the upper (lower) half of the complex ω-plane. The situation shown in Fig. 4 corresponds to an unstable mode.

These deliberations suggest the following modified Nyquist criterion: Consider the image curve of the positive half of the real axis $\omega = 0 \to \infty$ under the OLTF mapping in the $G(\omega)$-plane, as shown in Fig. 4. As one moves along the image curve in the direction of increasing frequency ω, an eigenmode with eigenfrequency ω_n is encountered each time the image curve passes the critical point -1 (in Fig. 4, only one sweep past an eigenfrequency is shown). If the critical point lies to the right of the image curve, the eigenmode is unstable, because then its frequency ω_n is located below the real axis in the ω-plane. On the other hand, if the critical point is located to the left, the eigenmode is stable. If the image curve passes through the critical point, the mode is neutrally stable.

In comparison to the classical Nyquist stability criterion, it is perhaps easier to foster an intuitive understanding of the modified Nyquist rule. However, it is admitted that no strict mathematical proof for the modified criterion is known. It has been validated successfully for a number of cases, where eigenfrequencies and growth rates can be determined by solution of the characteristic equation [42,43]. Nevertheless, one must concede that erroneous predictions may be obtained if the derivative of the OLTF vanishes for some real-valued frequency $\omega \in \mathbb{R}$ (the mapping is then not conformal). Furthermore, if an eigenfrequency has a large imaginary part such that the OLTF curve passes the critical point at a large distance, the proposed criterion may fail because conformality is a local property, i.e. it holds only in a finite-size neighborhood of the point considered. Fortunately, very large growth rates with $\Im(\omega) \ll 0$ are not observed in realistic network models, while very large damping rates with $\Im(\omega) \gg 0$ correspond to strongly damped modes, which are of no concern for the overall stability of a combustion system.

2.3. Identification of eigenfrequencies and growth rates from a Nyquist plot

Conformality, i.e. the local preservation of angles under a mapping $f : z \to f(z)$, implies that an orthogonal grid of lines with constant real or imaginary part, respectively, is mapped to an orthogonal grid of lines in the image plane (with the exception of points where the derivative of f is zero). In other words, under a conformal mapping, the neighborhood of any point is rotated and stretched or shrunk, as illustrated in Fig. 4. [47].

This interpretation of conformality implies that it is possible to estimate the frequency of an eigenmode ω_n as well as its rate of growth or decay from the image curve of the OLTF:

1. The real part $\Re(\omega_n)$ of the eigenfrequency is approximately equal to the frequency ω, where the distance between the image curve and the critical point attains a local minimum.

2. The absolute value of the imaginary part $\Im(\omega_n)$ is approximately equal to the minimum distance from the critical point to the OLTF image curve divided by the scaling factor of the mapping.

The scaling factor can be determined by evaluating how an interval $(\Re(\omega_n) - \Delta\omega; \Re(\omega_n) + \Delta\omega)$, is mapped to a segment $G(\Re(\omega_n) - \Delta\omega) \to G(\Re(\omega_n) + \Delta\omega)$ of the OLTF image curve. The scaling factor is then estimated as the arc length divided by $2\Delta\omega$ in the limit $\Delta\omega \to 0$. This geometrical approach for determining growth rates is particularly convenient if the OLTF is known in analytical form and can be evaluated continuously as a function of frequency ω. Further details on the procedure and example results for a semi-analytical test case are presented in Appendix C.

An alternative way of deducing the growth rate from the image curve has been proposed by Sattelmayer and Polifke, based on the identity theorem of functional analysis [44]. The theorem assures that a polynomial fit for the OLTF, which approximates the transfer function $G(\omega)$ with good accuracy for a range of purely real frequencies $\omega_1 \leqslant \omega \leqslant \omega_2$, with $\omega, \omega_1, \omega_2 \in \mathbb{R}$, will locally approximate the OLTF also for complex-valued frequencies $\omega \in \mathbb{C}$. This suggests to determine the growth rate of an eigenmode as follows: generate a polynomial fit $P_{G,m}(\omega) = g_m\omega^m + \cdots + g_0$ which approximates the OLTF curve close to the critical point, i.e. in the vicinity of an eigenmode ω_n, see Fig. 4. Then the frequency ω^* for which the approximating polynomial $P_G(\omega^*) = -1$ is determined with a numerical root finding algorithm. If the eigenmode ω_n is not too far away from the real axis, then $\omega_n \approx \omega^*$ with good accuracy. This approach is particularly convenient, if the OLTF is not known as a continuous function of frequency ω, but for a range of discrete frequencies, as it is the case for the OLTF derived from CFD simulation in the present work.

With the modified Nyquist criterion, complex-valued eigenfrequencies of an acoustical system can be determined from the OLTF image curve, which is computed for purely real frequencies $\omega \in \mathbb{R}$. This is very convenient when analytical expressions for transfer matrix coefficients are not known, which is usually the case for transfer matrices or response functions determined from experiment.

In concluding this section we remark that with the proposed rule for interpretation of Nyquist plots, it is obvious that the frequency at which the OLTF curve crosses the real axis should not be identified with an eigenfrequency. Indeed, it has been shown by example that this popular, but incorrect "heuristic" version of the Nyquist criterion does lead to erroneous predictions [43,48].

3. CFD-based determination of the open-loop transfer function

In the previous section it has been reviewed how the stability of a thermo-acoustic system can be deduced from a Nyquist plot. The Nyquist plot is usually generated from a network model of the system, which is "cut open" such that the open-loop transfer function can be computed from the model. This of course presumes that the transfer matrices of all two-ports, which comprise the system, are known. However, analytical expressions for transfer matrices are only known for particularly simple geometries. The determination of transfer matrices from experiment or CFD, on the other hand, is difficult, error-prone and time-consuming [35,36,49].

In this section a hybrid method, combining CFD and network models, for computation of the OLTF is introduced. The approach is suitable for systems where a complete low-order network formulation is not appropriate or not available – due to geometrical complexities or non-compact regions of heat release, etc., or simply because not all required transfer matrices are explicitly known. It is emphasized that it is not the purpose of the CFD model to determine two-port transfer matrices or heat source transfer functions (cf. [36,50]). Indeed, explicit knowledge of these quantities is not required for stability analysis with the Nyquist criterion.

In the following the general strategy of the proposed approach is exemplified by a simple combustion system, then expected advantages and areas of application are discussed.

3.1. Outline of the method

Consider a combustion system comprised of a long plenum, burner and combustion chamber as shown in Fig. 5. The acoustic boundary condition at the upstream end of the plenum is given in terms of a complex-valued, frequency-dependent impedance $Z(\omega) = \hat{p}(\omega)/\hat{u}(\omega)$. At the combustor exit, an "open end" boundary condition with $p' = 0$ is assumed.

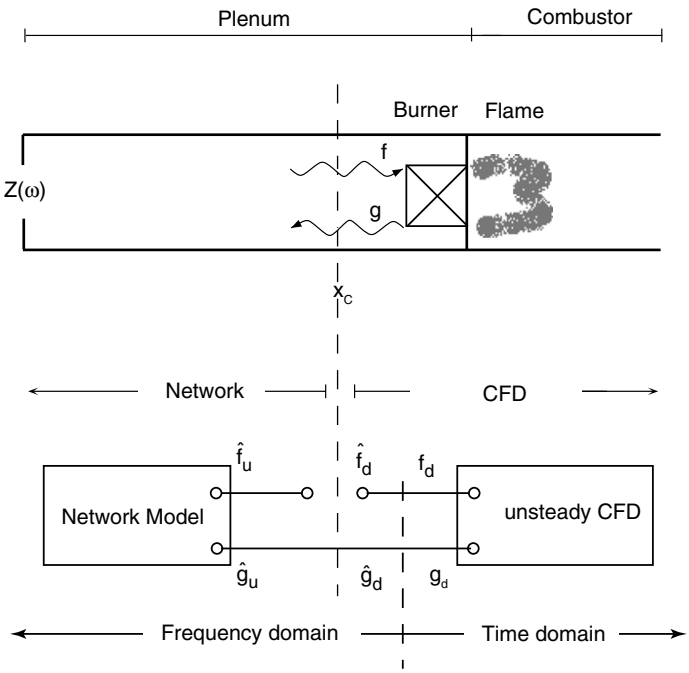

Fig. 5. The hybrid approach for determination of the OLTF. Top: combustion system with plenum, burner, flame, combustion chamber and combustor exit. Bottom: System-model comprised of CFD-module (left) and network-module (right). The OLTF is obtained as $G = -\hat{f}_u/\hat{f}_d$.

For the sake of argument it is assumed that the transfer matrix of the burner and the frequency response of the flame to acoustic perturbations are not known. In this case, burner and flame as well as the combustor should be modeled with CFD, using an appropriate formulation for unsteady, turbulent, reacting flow. At the downstream boundary of the computational domain, i.e. at the combustor exit, a constant pressure boundary condition is applied. As indicated in Fig. 5, the computational domain of the CFD model begins at some location x_C upstream of the burner. Here boundary conditions are imposed which are acoustically non-reflecting, and at the same time allow to impose an external perturbation $f_d(t)$. If a broad-band excitation signal is applied, a simulation extending over a few periods of the lowest frequency of interest generates time series data, which provide after fast Fourier transform (FFT) the acoustic output $\hat{g}_d(\omega)$ to the input $\hat{f}_d(\omega)$.

The ratio $\hat{g}_d(\omega)/\hat{f}_d(\omega)$ can be interpreted as the frequency response of burner and combustor (including the flame), but it must not be identified with the OLTF of the system. Therefore the data from the CFD run alone are not sufficient to assess the stability of the system. However, modeling the elements upstream of the location x_C with a network model, the response $\hat{f}_u$ to the excitation $\hat{g}_u = \hat{g}_d$ can be computed. The open-loop transfer function of the system can now be determined as $G(\omega) = -\hat{f}_u(\omega)/\hat{f}_d(\omega)$, stability analysis and identification of eigenfrequencies is then carried out as outlined above. A flow chart of this procedure is shown in Fig. 6. As in Fig. 5, it is indicated which part of the overall model "lives" in the time domain and the frequency domain, respectively.

It should be obvious after what has been said that the interface at x_C between the CFD model and the network model is equivalent to the diagnostic dummy of a full network model, i.e. the system is "cut open" at this location. It is indeed essential that a part of the system is represented by a network model, such that the "cut" can be implemented and an assessment of the stability against self-excited instability be made based on computational results obtained with external excitation.

3.2. Further remarks on the proposed method

In the previous sub-section, the basic idea of the CNN approach has been introduced. The central motivation for the present paper is to establish proof of concept for the method by validating against a simple test

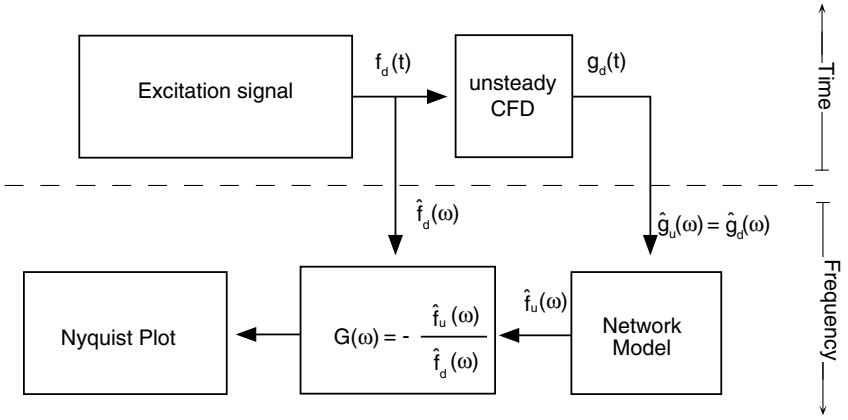

Fig. 6. Flow chart for CFD-based determination of the OLTF.

case, i.e. a duct with an acoustically compact, time-lagged heat source – similar to a Rijke tube. For such a system, the eigenmodes and the stability properties may be computed by a simple network model (or even by a semi-analytical approach, see Appendix C), which is very convenient for a validation study.

However, for a configuration as simple as a Rijke tube, the CNN approach is unnecessarily complicated. Therefore, we present in the following miscellaneous comments on possible areas of applications and expected advantages of the CNN approach. At the time of writing, we cannot yet substantiate all the claims made below, because the application of the method to more realistic configurations – including combustion and large eddy simulation – is the subject of ongoing work.

- Depending on the problem under investigation, the CNN method can certainly be applied to configurations other than the one sketched in Fig. 5. It may be appropriate to model the upstream part of the overall system in CFD, with the network model representing the downstream part. This could be advantageous, for example, if a long chimney is located downstream of a combustion chamber. In general, the network submodel should be used to represent those parts of the system for which transfer matrices are known. This could be a tubular or annular combustion chamber, a long chimney, or an air supply duct, etc.On the other hand, it is readily admitted that there are certainly configurations, for which the CNN method is not suitable. One example for this would be geometries so complex that a "cutting plane" with normal incidence of acoustic waves cannot be identified.
- It can be expedient to reduce the network model to only the downstream or upstream boundary condition. In this way, it is not necessary to implement a boundary condition that represents a complex-valued, frequency-dependent impedance or reflection factor in the CFD model.
- Advanced CFD models, in particular large eddy simulation, do in principle take into account all important flame–acoustics interactions, even vortical or entropy modes. Complicated geometries can be considered without essential difficulty, as long as they are represented by the CFD sub-model. In this sense, the proposed model is comprehensive.
- The proposed method is also comprehensive in the sense that both unstable as well as stable eigenmodes are detected. This is an advantage over transient CFD simulation of system development from a perturbed initial state, where one can identify in general only the dominant unstable mode that develops during the course of the simulation. Furthermore, for the latter approach it is required to represent the complete system in the CFD model. This can be computationally very expensive, and requires to implement the correct acoustic boundary conditions in the CFD model, which is a difficult problem in its own right.
- A further advantage over transient CFD-simulation from a perturbed initial state is the following: the self-excited growth of initially small perturbations into a fully developed mode with distinct eigenfrequency can run over many oscillation cycles, consuming huge amounts of computer resources. On the other hand, with the CNN approach the external forcing in combination with the non-reflecting acoustic boundary leads to a

quasi-steady, oscillatory state comparatively quickly. It follows that compute times, which correspond to only a few cycles of the lowest frequencies of interest, are sufficient to assess the stability of the combustor.

- It is not required that the boundary condition at x_C in the CFD model is fully non-reflecting. If there is partial reflection – which is the case for the widely used characteristics-based boundary conditions proposed by Poinsot and Lele [14,15] – one simply has to identify acoustic signal components f_d, g_d propagating in the upstream and downstream direction, respectively, a short distance away from the boundary of the computational domain.
- It has been proposed to use CFD in combination with tools from system identification (SI) to determine the frequency response or the transfer matrix of a flame, say, and then use this information to build a complete system model for stability analysis [21,28,33,36,37,50]. Obviously there are commonalities and important differences between this "CFD/SI" approach and the CNN method presented here. The latter could be more suitable for systems where due to geometrical complexities, multi-stage fuel injection, or acoustically non-compact regions of heat release, the representation of the flame dynamics as a single-input/single-output flame transfer function is not appropriate. For example, when considering a premix burner with "practical premixing" (i.e. the fuel injector is not acoustically decoupled from the combustion chamber), a premix flame should in general be represented as a multiple-input/single-output (MISO) element [33]. Alternatively, the burner transfer matrix, which is a multiple-input/multiple-output (MIMO) element, can also be identified. Identification of MISO or MIMO elements generates additional – although not insurmountable – complexity for the CFD/SI approach and requires longer times series for robust estimation. Contrary to that, with CNN the CFD sub-model is always considered as a single-input/single-output (SISO) system, which should make the determination of the OLTF comparatively robust and computationally less demanding. Nevertheless, the impact of the fuel injector impedance on the combustion stability, say, should be taken into account quite naturally, if the fuel injector is part of the CFD sub-model. Further experience with both the CFD/SI and the CNN method and comparative validation studies are needed to better understand strengths and weaknesses of the two approaches.
- The CNN approach is also promising for applications involving elements with non-linear transfer-behavior (e.g. a flame at large amplitudes of oscillation). For this situation, Stow and Dowling [51] have presented a low-order method which combines a simple non-linear flame model with an otherwise linear network model of a combustor in order to determine limit cycle amplitudes. The approach is intriguing, but to derive a realistic non-linear flame transfer function remains a challenging task. With the proposed hybrid approach, only the part of the system including the non-linear element would be modeled with CFD.

For proof-of-concept of the new hybrid method, it has been applied to a simple, one-dimensional model of a Rijke tube, cf. [36]. Before representing the results achieved, the physics and the linear stability analysis of a Rijke tube are reviewed in the next sections.

4. Physics of the Rijke tube

The Rijke tube is perhaps the most simple system that can exhibit self-excited thermo-acoustic instability. It has been described in great detail in the literature [11,45,46,52,53], only a short summary of the instability mechanism is given here. A Rijke tube consists of a straight duct with a wire gauze inside. If the wire gauze is heated – either electrically, or by exposing it to a flame – and air flows through the duct due to free or forced convection, the Rijke tube can produce intense sound. Acoustic fluctuations within the duct reach amplitudes of up to several hundred Pascal, depending on the position of the gauze and the boundary conditions at the ends of the duct. The frequency of fluctuation is in general close to one of the "organ pipe" eigenmodes of the duct.

According to Rayleigh [2], instability in a thermo-acoustic system may occur "If heat be given to the air at the moment of greatest condensation", i.e. highest density. In simplest terms, this condition can be formulated mathematically as follows:

$$\text{Instability is possible, if } \int_{t_0}^{t_0+2\pi/\omega} \dot{Q}'(t)p'(t)\mathrm{d}t > 0, \tag{10}$$

where $\dot{Q}'(t)$ denotes deviations from the mean rate of overall heat release $\overline{\dot{Q}}$ (units W) such that $\dot{Q}(t) = \overline{\dot{Q}} + \dot{Q}'(t)$, and similarly for pressure.

The Rayleigh criterion Eq. (10) expresses the idea that acoustic energy can be generated by the interaction of unsteady heat release and acoustic fluctuations, if fluctuations of heat release and pressure, respectively, are at least to some extent phase aligned. This is possible in the Rijke tube, because transfer of heat from the hot wire mesh to the air passing through the mesh does not respond instantaneously, but with a certain time-lag τ to a change in the flow velocity u. Indeed, according to King [46,54,55], the heat flux from a hot wire with length L_W, diameter d and temperature T_W to a gas flowing past it with velocity $u(t)$ and temperature T can be calculated as

$$\dot{Q}(t) = L_W(T_W - T)\left(\lambda + 2\sqrt{\pi\lambda\bar{\varrho}c_v\frac{d}{2}|u(t-\tau)|}\right). \tag{11}$$

Here $\bar{\varrho}$ is the mean density, c_v the specific heat per unit mass at constant volume and λ the heat conductivity of the gas. According to Lighthill [55] the time lag may be estimated as

$$\tau \approx 0.2\frac{d}{\bar{u}} \tag{12}$$

for frequencies $f \ll 20\bar{u}/d$, which holds for all frequencies regarded in this work.

For the fundamental acoustic eigenmode in a duct of length l with two open ends $p(0) = p(l) = \text{const.}$, see Fig. 7, the pressure fluctuations lag behind the velocity fluctuations with a phase angle of $\pi/2$ in the upstream half of the tube, while they are ahead of the velocity fluctuations with a phase angle of $\pi/2$ in the downstream half. Thus, if the gauze is placed in the upstream half of the tube, the phase angles of heat release and pressure oscillations both follow after the phase angle of the velocity fluctuations. For a typical Rijke tube, the time lag τ is smaller than one quarter period of the first eigenmode $\omega\tau < \pi/2$, thus, $\dot{Q}'(t)$ and $p'(t)$ are not exactly in phase. However, as long as $0 < \omega\tau < \pi$, heat release will be phase aligned to some extent with pressure and vice versa. Thus, a self-excited oscillation results. The amplitude increases until non-linear effects cause the augmentation to vanish and a limit cycle is reached. Non-linear effects include the heat release at high amplitudes and losses at the ends of the tube [46].

If the heating mesh is placed in the downstream half of the tube, the Rijke tube does not exhibit self-excited instability. Pressure oscillations are out of phase with heat release oscillations, fluctuations become attenuated.

For higher order modes, the analysis is more involved, but the fundamental mechanism is the same: if heat release and pressure fluctuations lead to a positive Rayleigh integral (i.e., they are at least somewhat in phase), the mode will be excited; if the Rayleigh integral is negative, the mode is damped.

5. Network model of the Rijke tube

In the following paragraphs, we will show how to model the Rijke tube depicted in Fig. 7 as a network of two-port elements. For convenience, the model is constructed with the characteristic wave amplitudes f and g (“Riemann Invariants”) instead of the “primitive acoustic variables” velocity u' and pressure p'. The wave amplitudes f and g represent waves propagating in the down- and upstream direction, respectively. They are related to the primitive acoustic variables as follows,

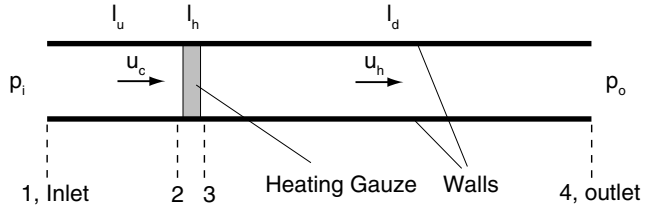

Fig. 7. A Rijke tube with two open ends and the heating wire gauze at 1/3 position.

$$f = \frac{1}{2}\left(\frac{p'}{\bar{\varrho}\bar{c}} + u'\right), \quad g = \frac{1}{2}\left(\frac{p'}{\bar{\varrho}\bar{c}} - u'\right). \tag{13}$$

The upstream boundary condition of the network is an open end with constant pressure p_i, thus $p' = 0$. From Eq. (13) it follows that at node "1" of the network

$$f_1 + g_1 = 0. \tag{14}$$

The next element of the model is a straight duct of length l_u. A downstream traveling wave f undergoes a change in phase $\exp\{-i\omega l_u/c_c\}$ as it travels with the speed of sound $c_c = \sqrt{\kappa R T_c}$ from the inlet to the cold side of the heat source. The index "c" stands for the "cold" side of the Rijke tube. The case for the wave g traveling in the upstream direction is similar. Along the length of the duct, there is no interaction between the waves f and g. The transfer matrix of the duct is readily obtained:

$$\begin{pmatrix} f_2 \\ g_2 \end{pmatrix} = \begin{pmatrix} e^{-ik_c l_u} & 0 \\ 0 & e^{ik_c l_u} \end{pmatrix} \begin{pmatrix} f_1 \\ g_1 \end{pmatrix}, \tag{15}$$

with the wave number $k_c \equiv \omega/c_c$. Mean flow and dissipative effects have been neglected, as they are important only at higher Mach numbers and when wave propagation over long distances is considered, respectively. However, it would be possible to incorporate these without essential difficulty.

The extent of the heat source in longitudinal direction is negligible and it will be assumed that $l_h = 0$. The pressures and velocities on the cold and hot sides of the wire gauze, respectively, can then be related to each other via the Rankine–Hugoniot equations for conservation of mass, momentum and energy across a thin heat source [56]. Linearising those for p' and u', coupling relations for the fluctuations across the heat source can be derived (see Appendix A for the complete derivation):

$$\begin{aligned} p'_3 &= p'_2 - \varrho_c u_c^2 \theta \left(\frac{u'_2}{u_c} + \frac{\dot{Q}'}{\bar{\dot{Q}}}\right), \\ u'_3 &= u'_2 + u_c \theta \left(\frac{\dot{Q}'}{\bar{\dot{Q}}} - \frac{p'_2}{p_c}\right), \end{aligned} \tag{16}$$

with temperature excess $\theta \equiv (\overline{T_h}/\overline{T_c} - 1)$. Linearising $\dot{Q}$ from Eq. (11) for small fluctuations (see Appendix B) yields

$$\frac{\dot{Q}'}{\bar{\dot{Q}}} = \frac{u'_2 e^{-i\omega\tau}}{\lambda\sqrt{\frac{u_c}{C_1}} + 2u_c}, \tag{17}$$

with $C_1 = \pi\lambda c_v \varrho d/2$. Finally, one obtains the transfer matrix for the characteristic wave amplitudes across the heat source

$$\begin{pmatrix} f_3 \\ g_3 \end{pmatrix} = \frac{1}{2}\begin{pmatrix} A - B + C - D & A + B - C - D \\ A - B - C + D & A + B + C + D \end{pmatrix} \begin{pmatrix} f_2 \\ g_2 \end{pmatrix}, \tag{18}$$

with

$$\begin{aligned} A &= \frac{1}{\xi}, \quad B = \frac{M_c \theta}{\xi}\left(1 + \frac{e^{-i\omega\tau}}{2 + \lambda/\sqrt{C_1 u_c}}\right), \\ C &= \left(1 + \frac{\theta e^{-i\omega\tau}}{2 + \lambda/\sqrt{C_1 u_c}}\right), \quad D = \gamma M_c \theta. \end{aligned} \tag{19}$$

Here $\xi \equiv \varrho_h c_h/\varrho_c c_c$ denotes the ratio of specific impedances and $\gamma \equiv c_p/c_v$ the ratio of specific heats.

Downstream of the heat release follows another straight duct with length l_d and thus

$$\begin{pmatrix} f_4 \\ g_4 \end{pmatrix} = \begin{pmatrix} e^{-ik_h l_d} & 0 \\ 0 & e^{ik_h l_d} \end{pmatrix} \begin{pmatrix} f_3 \\ g_3 \end{pmatrix}, \tag{20}$$

with the wave number $k_h \equiv \omega/c_h$ in the hot section of the duct.

Finally, in order to close the system of equations, one more relation is required which is delivered by the open end boundary condition at the downstream end of the Rijke tube:

$$f_4 + g_4 = 0. \tag{21}$$

From Eqs. (14)–(21) for the unknowns $(f_1, g_1, f_2, \ldots, g_4)$ an 8×8 system matrix $\mathbf{S}$ can be constructed. Then the characteristic equation $\mathrm{Det}(\mathbf{S}) = 0$ is solved for eigenmodes ω_n.

6. Numerical simulations

In order to establish proof of concept for the CNN approach, the method has been applied to the model of a Rijke tube as discussed in the previous section.

The thermo-acoustic stability of a Rijke tube has been investigated previously with CFD by Hantschk and Vortmeyer, using a two-dimensional mesh to resolve the flow and heat transfer at a heating strip with specified wall temperature [11]. The rate of heat transfer to the fluid and in particular the response to a perturbation of the flow velocity was computed by the CFD model from the governing equations for mass, momentum and energy in viscous, wall-bounded, laminar flow.

For the present purposes it is not necessary to resolve flow and heat transfer at the gauze in this manner. Instead, a one-dimensional model is set-up, with the heating gauze represented as a "lumped parameter" source term for the enthalpy transport equation, cf. [36]. A time lag τ between a change in velocity and the strength of the enthalpy source term is implemented by storing the time series $u(t)$ of velocity at a location just upstream of the region of heat release in computer memory. The momentary rate of heat release $\dot{Q}(t)$ is then computed as a function of the earlier velocity $u(t-\tau)$ according to Eq. (11). Note with such a formulation, the time lag τ is not predicted by the CFD model, but an adjustable parameter.

6.1. Set-up of the CFD model

For the geometry considered, it is convenient to include the heat source and the downstream duct in the CFD domain, while representing the upstream duct with a network model, see Fig. 8. In this way, one can easily investigate the effect of upstream boundary condition and upstream duct length on stability (see below).

A typically dimensioned Rijke tube was chosen as a reference case. The computational domain for CFD is divided into sections of length $l_c = 10$ mm and $l_h = 495$ mm upstream and downstream of the region of heat release, respectively. All other parameters too, are set to represent a typical Rijke tube. The mean cold air velocity at the inlet is set to $\bar{u} = 0.6$ m/s and the inlet temperature to 293 K, while the mean heat release rate is dimensioned in a way to generate a hot air temperature of 500 K to ensure sufficient acoustical excitation. A typical wire diameter in a real Rijke tube is 0.5 mm, resulting in a time lag of $\tau = 1.67 \times 10^{-4}$ s according to Eq. (12). In order to avoid discontinuities of flow variables and convergence difficulties, the heat source is not implemented as a point source, but "smeared out" over a region of length $l_{\dot{Q}} = 10$ mm, i.e. 10 computational cells, with maximal heat release rate in the center of that region. Except for unrealistically high modes, $l_{\dot{Q}}$ is very short compared to the acoustical wave length and the heat source can be considered to be acoustically compact, which was assumed in the derivation of the Rankine–Hugoniot relations Eq. (16).

The CFD solver Fluent used in this study does not allow one-dimensional computations, therefore a quasi-one-dimensional mesh with uniform cell size of 1×1 mm has been created. Consistent with the inviscid flow model employed, slip boundary conditions are implemented at the upper and lower boundaries. Invoking the "pressure far-field" boundary condition of Fluent,[3] an acoustically non-reflecting boundary condition (NBC) is used for the inlet (left side) of the CFD model and constant pressure with $p' = 0$ (acoustically "open end") is assumed for the outlet (right side).

With the non-reflecting boundary condition, a self-excited instability cannot develop in the CFD mode (as was the case in the work of Hantschk and Vortmeyer [11]). Therefore it is easy to generate a stationary

[3] Test simulations confirmed for 1-D geometries and Eulerian (inviscid) flow a reflection factor for this type of boundary condition of effectively 0. Other frequent problems of NBCs like drifting mean pressure due to an under-determined system were not observed either.

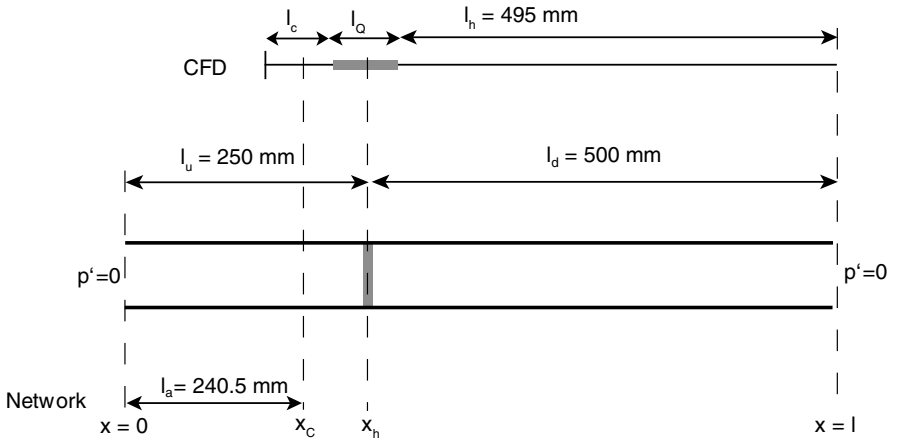

Fig. 8. Configuration of Rijke tube with open/open boundary conditions and heating gauze placed one third of the tube length downstream from the inlet. Relevant dimensions of the CFD and the network model are also shown above and below, respectively, of the sketch of the tube. The "cut" between the CFD and the network domain is at $x = x_C$.

solution for the inviscid Euler equations, which can then be used as a starting point for simulations with external excitation.

6.2. Results of the simulations with external excitation

For computation of the OLTF, the inlet boundary of the CFD model is perturbed with a sum of discrete harmonic acoustic signals[4]

$$f_d(t) = \sum_i a_i \sin(2\pi f_i t + \phi_i), \tag{22}$$

with frequencies f_i ranging from 50 to 3000 Hz in steps of $\Delta f = 50$ Hz, amplitudes $a_i = 6 \times 10^{-3}$ m/s and a random phase offset ϕ_i (random number between 0 and 2π) for each frequency. The resulting amplitudes for the primitive variables are 3×10^{-3} m/s for u' and 1.24 Pa for p', respectively. Such low amplitudes in the discrete signals were chosen because the peak amplitude in the overall signal (sum of sinusoids) even with the use of a random phase lag reaches up to the 17-fold of the amplitudes of the discrete sinusoids. This way the maximum peak amplitude for u' is kept below 8.5% and thus below the critical value of one third of the mean flow velocity, above which non-linear effects become significant according to Heckl [46].

The incoming characteristic wave f_d as well as the outgoing signal g_d have been determined via Eqs. (13) by monitoring pressure p and axial velocity u at a location $x_C = 4.5$ mm, i.e. in the fifth cell of the computational domain and upstream of the region of heat release. The simulated virtual time (and so the length of the time series recorded) was of the order of 0.3 s, long enough to let transition effects from the onset of excitation leave the domain and also long enough for a robust frequency analysis. The solver used for the simulations must not have any discernible dissipation or dispersion of acoustic signals, which could be realized by application of the coupled explicit solver option in Fluent. Both signals were then processed with fast Fourier transformation (FFT) delivering amplitude and relative phase of each sinusoid present. It should be emphasized, that judging from our experience the length of the time series so processed has to be a multiple of $1/\Delta f$ to enable a numerically stable and exact determination of the FFT. Due to the explicit solver chosen, the maximum possible time step was determined by $CFL = 1$ to avoid divergence. The resulting physical time step in the simulation was of the order of 1.1×10^{-6} s, leading to a Nyquist frequency of about 450 kHz, significantly above any frequency of interest in the present context. On a 64-Bit dual-core processor computer with 2 GHz, 300,000 time steps – corresponding to 0.3 s elapsed time – required about 2:30 h.

[4] In Fluent, the excitation is realized by perturbing the Mach number at the non-reflecting inlet.

6.3. Open end on the left side

The eigenfrequencies of a Rijke tube with two open ends and the heating mesh positioned at 1/3 of the overall duct length were calculated with the CNN approach as explained above.

In order to compute the OLTF of the Rijke tube, one must compute how the output $\hat{f}_u(\omega)$ of the network model is related to the input $\hat{g}_u(\omega)$. For the Rijke tube considered, the network sub-model is very simple: it is a duct of length $l_a = 240.5$ mm, as shown in Fig. 8, with an "open end" with $p' = 0$ as boundary condition. An acoustic wave traveling from the "cut" at x_C to the upstream end of the tube experiences a phase shift of π at the open end before traveling back over the length l_a to the cut. Thus,

$$f_u(\omega) = g_u(\omega)\mathrm{e}^{-\mathrm{i}(k_c 2l_a+\pi)}. \tag{23}$$

With this method, the OLTF for the above mentioned frequencies can be calculated. Fig. 9 shows the OLTF for the range of $f = 100$–400 Hz (for the sake of clarity, the complete OLTF has not been shown here). The frequency gap of 50 Hz between the signals is too large to decide whether the OLTF image curve passes to the right or to the left of the critical point -1. Also, the frequency spacing is too large for curve fitting of the OLTF and thus calculation of the eigenfrequencies. Nevertheless, the plot suggests that an eigenfrequency should be found in the region between 250 Hz and 300 Hz. Hence a second simulation is set-up with external forcing by a sum of sinusoids in the frequency range 250–300 Hz in steps of 10 Hz and an amplitude of 0.005 m/s. Amplitudes of the excitation signal sent into the domain were again kept low, in order to make sure that the linear regime is not left.

From the outgoing signal, the OLTF is calculated with higher frequency resolution, see Fig. 9, right side. Now one can deduce from the plot that an unstable eigenmode exists with frequency slightly above 270 Hz, since the critical point -1 lies to the right of the OLTF curve. A 4th order polynomial fit $G_{250}(\omega)$ is calculated from the results of the second CFD simulation. This polynomial fit is an approximation of the function $G(\omega)$ in the area around the frequencies 250–300 Hz. With a root finding algorithm, the equation $G(\omega) = -1$ can now be solved for ω (or physical frequency f respectively). In this way, the first unstable mode $f_1 = 271.51 - 1.83i$ of the Rijke tube with a growth rate of 4.32% is found.

In order to validate the modes calculated with the CNN method, eigenfrequencies for the Rijke tube as shown in Fig. 8 were determined by solving the characteristic equation of a network model, which can be considered to give exact solutions for the present configuration, while it is particularly easy to set-up, see Section 5. Apart from the values already mentioned in Section 6, the following parameter settings were used, which can be derived from the inlet conditions and the heat flux: $u_c = \bar{u} = 0.6$ m/s, $u_h = 1.02$m/s, $p_c = 101325$ Pa, $\varrho_c = \bar{\varrho} = 1.205$ kg/m^3, $\varrho_h = 0.705$ kg/m^3, $c_c = 343$ m/s and $c_h = 448$ m/s. The result for the first eigenfrequency is $f_{nw,1} = 271.06 - 1.67i$ with a growth rate of 3.94%. Thus, the results obtained with the new method are validated with excellent accuracy.

This procedure is repeated for all frequencies where the OLTF passes the critical point.

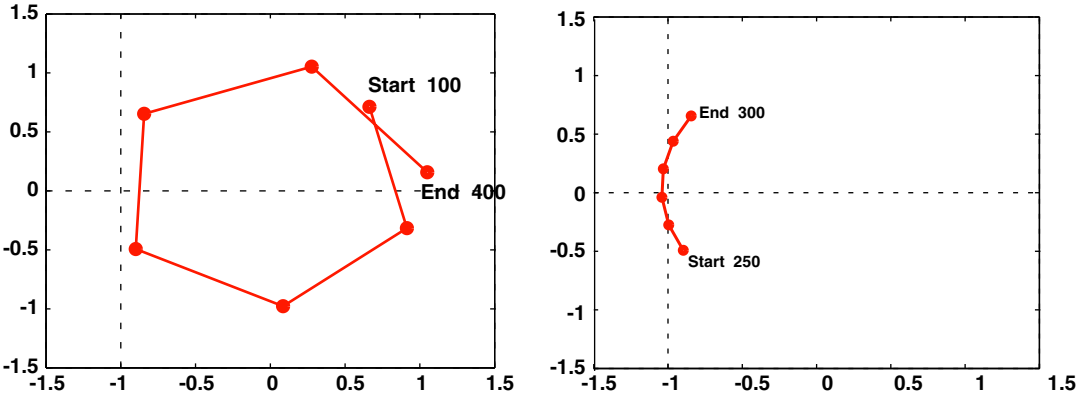

Fig. 9. OLTF of the Rijke tube. Left: large frequency spacing; Right: fine frequency spacing.

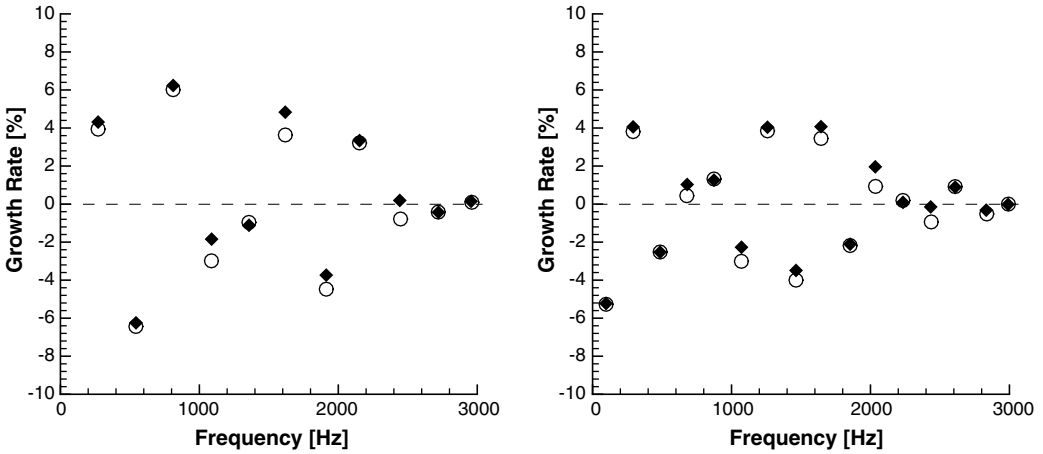

Fig. 10. Comparison of eigenfrequencies and growth rates of a Rijke tube with $x_h/l = 1/3$ and open end upstream boundary condition (left), $x_h/l = 1/2$ and closed end upstream boundary condition (right). ○ – network model: ♦ – CNN.

A comparison of CNN vs. network model results is depicted in Fig. 10, left side (for completeness, the numerical values of the eigenfrequencies are listed in Table D.1 in Appendix D). All eigenmodes calculated with the network model have been identified by the CNN method. It is emphasized that the loci of the eigenmodes depicted in the plot have two degrees of freedom, i.e. the frequency (in Hz) and the growth rate (in percent per cycle). It is seen that the frequencies are in very good agreement, but also the growth rates from the CNN method are close to the values calculated with the network model. The stability characteristics (stable/unstable corresponding to negative or positive growth rate) of every mode is captured correctly, with the exception of the 9th mode at approx. 2450 Hz for the case with $x_h/l = 1/3$ and open end upstream boundary (left graph). However, this small discrepancy is not very significant: the 9th mode is almost neutrally stable, overall system behavior will be dominated by the unstable modes (1st, 3rd, 6th and 8th mode).

In experiment, the first eigenmode is usually observed in a Rijke tube. According to our analysis, this mode is not the one with the highest growth rate (dominant unstable mode). The oversimplified treatment of the boundaries in our validation test case can account for this result: Ideal acoustic boundary conditions with a reflection factor $|r| = 1$ were chosen, while it is well known that radiation losses of acoustic energy occur at an open pipe end, and in particular so for higher frequencies. Without these losses, the third mode can have a higher growth rate than the first mode, since the small time delay τ suits better for the higher frequency in a sense of bringing pressure and heat release fluctuations better in line. In reality, higher order modes will have comparatively more losses and therefore smaller growth rates than the fundamental unstable mode.

6.4. Closed end on the left side

In a second set of computations, the modes for a Rijke tube with a closed inlet (fixed velocity) and an open outlet were determined by both methods. The heating gauze is positioned in the center of a tube of length 1 m. Thus, a length $l_a = 490.5$ mm results for the analytical part of the OLTF computation. Furthermore, a different upstream boundary condition is implemented. For the network model, Eq. (14) reads now

$$f_1 - g_1 = 0. \tag{24}$$

For computation of the OLTF, Eq. (23) is simplified to

$$f_u(\omega) = g_u(\omega)\mathrm{e}^{-\mathrm{i}(k2l_a)}, \tag{25}$$

without the phase change of π. Note that this different acoustic boundary condition did not require any changes to the computational set-up for the CFD part of the overall mode (see Fig. 11).

The eigenfrequencies for this problem set-up were approximately identified from CFD data obtained with broad-band excitation in the frequency range from 50 to 3000 Hz. Note that for this part of the analysis, it is

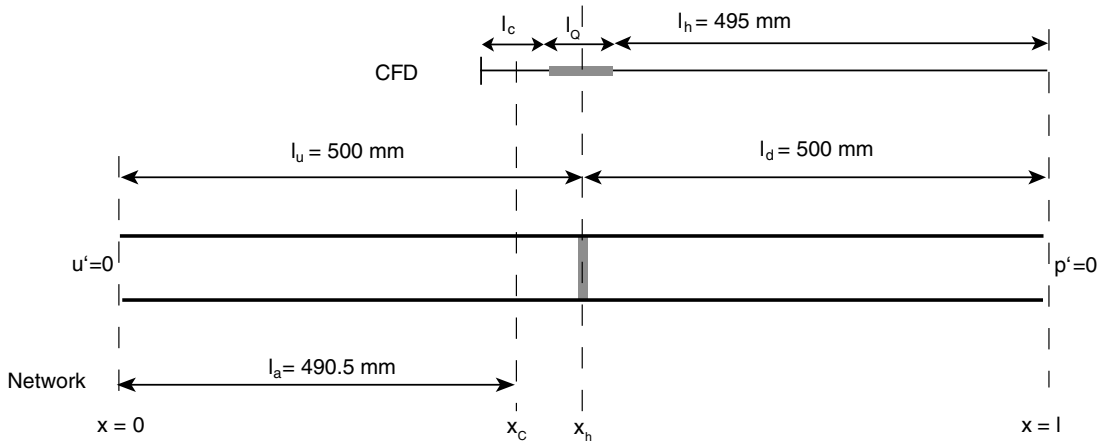

Fig. 11. Configuration of Rijke tube with closed/open boundary conditions and heating gauze placed in the middle of the duct. Relevant dimensions of the CFD and the network model are also shown above and below, respectively, of the sketch of the tube. The "cut" between the CFD and the network domain is at $x = x_C$.

possible to re-use the data that were generated for analysis of the open-end-on-the-left configuration discussed in the previous sub-section, because the CFD-part of the overall model is unchanged. Then additional simulations with higher frequency resolution were performed to determine precise values for the eigenfrequency and to determine stability. Again, results were validated by comparison with a network model, see Fig. 10, right side (and Table D.2 in Appendix D). Again, all modes are correctly identified, the frequencies are captured very accurately and the deviations for the growth rates are very small.

7. Conclusions and outlook

A hybrid "CNN" method for the determination of thermo-acoustic system stability has been proposed, combining tools and concepts from computational fluid dynamics, network models of linear acoustics and control theory.

To establish proof of concept, the novel method has been applied to an idealized model of a Rijke tube. For this model problem, numerical solutions of a low-order "network model" may be regarded as an exact reference solution. Both stable as well as unstable eigenmodes have been identified with CNN over a wide range of frequencies for two configurations considered. The frequencies of all modes are captured very accurately, the growth rates computed are in good agreement with results of the network model.

The proposed approach is particularly appropriate for applications where (1) the frequency response or the transfer matrix of important elements cannot be determined and (2) the network approach is not adequate due to geometrical complexities. CNN is also suitable for configurations with non-trivial acoustic boundary conditions – in general a frequency-dependent, complex-valued impedance, which is not readily realized in a CFD code – if that boundary is located in the network part of the system model. Moreover, the method can be used for the determination of eigenfrequencies and growth rates of any kind of acoustic resonator, not only of thermo-acoustic systems.

To summarize, the proposed CNN method for stability analysis has been validated successfully and possible areas of application have been identified. Ongoing work is concerned with more complicated configurations, including turbulent combustion, use of large eddy simulation for the flow simulation, as well as comparison against experimental results.

Acknowledgments

The authors thank Dr. Maria A. Heckl for providing details about her Rijke tube model. Financial support was provided by Deutsche Forschungsgemeinschaft, Project Po 710/3-1.

Appendix A. Linearization of the Rankine–Hugoniot equations

For one-dimensional, compressible flow across a compact source of heat, the conservation equations for mass, momentum and energy, respectively, are

$$\rho_h u_h = \rho_c u_c, \tag{A.1}$$

$$p_h + \rho_h u_h^2 = p_c + \rho_c u_c^2, \tag{A.2}$$

$$h_h + \frac{1}{2}u_h^2 = h_c + \frac{1}{2}u_c^2 + q, \tag{A.3}$$

where q is specific intensity of the heat source (units J/kg).

For an ideal gas with $p = \rho RT$ and speed of sound $c^2 = \kappa RT$, where $\kappa \equiv c_p/c_v$ is the adiabatic exponent, one finds that

$$c^2 = \kappa \frac{p}{\rho} \tag{A.4}$$

and

$$\left(\frac{c_h}{c_c}\right)^2 = \frac{T_h}{T_c}. \tag{A.5}$$

Enthalpy $h \equiv c_p T = c_v T + p/\rho$ and it follows that

$$h = \frac{p}{\rho}\frac{c_p}{c_p - c_v} = \frac{p}{\rho}\frac{\kappa}{\kappa - 1}. \tag{A.6}$$

Applying Eq. (A.6) to Eq. (A.3), the energy equation transforms to

$$\frac{p_h}{\rho_h}\frac{\kappa}{\kappa - 1} + \frac{1}{2}u_h^2 = \frac{p_c}{\rho_c}\frac{\kappa}{\kappa - 1} + \frac{1}{2}u_c^2 + q. \tag{A.7}$$

With Eq. (A.4) one writes

$$\frac{c_h^2}{\kappa - 1} + \frac{1}{2}u_h^2 = \frac{c_c^2}{\kappa - 1} + \frac{1}{2}u_c^2 + q, \tag{A.8}$$

and finally

$$\frac{c_h^2}{c_c^2} = \frac{\frac{1}{2}(u_c^2 - u_h^2) + q}{c_c^2}(\kappa - 1) + 1. \tag{A.9}$$

Assuming low Mach number (i.e. $u_c < u_h \ll c_c$) and employing (A.4), this reduces to

$$\frac{c_h^2}{c_c^2} = 1 + \frac{q\rho_c}{p_c}\frac{(\kappa - 1)}{\kappa} + \mathcal{O}(M^2). \tag{A.10}$$

With $\dot{q} = \rho_c u_c q$ (heat released per unit area, units W/m^2), one arrives at a relation between the speed of sound of hot and cold gases

$$\frac{c_h^2}{c_c^2} = 1 + \frac{\dot{q}}{p_c u_c}\frac{(\kappa - 1)}{\kappa} + \mathcal{O}(M^2). \tag{A.11}$$

In a similar manner, one finds a coupling condition for the velocities. Rearranging Eq. (A.2)

$$\frac{p_h}{\rho_h} + u_h^2 = \frac{p_c}{\rho_h} + \frac{\rho_c}{\rho_h}u_c^2, \tag{A.12}$$

employing mass conservation (A.1) and (A.4), one finds

$$\frac{c_h^2}{\kappa} + u_h^2 = \frac{c_c^2 u_h}{\kappa u_c} + u_h u_c \tag{A.13}$$

or

$$\frac{c_h^2}{c_c^2}+\frac{u_h^2}{c_c^2}\kappa-\frac{u_c u_h}{c_c^2}=\frac{u_h}{u_c}, \tag{A.14}$$

which, inserting Eq. (A.11), finally yields

$$\frac{u_h}{u_c}=1+\frac{\dot{q}}{p_c u_c}\frac{(\kappa-1)}{\kappa}+\mathcal{O}(M^2). \tag{A.15}$$

Rearranging Eq. (A.2) yields for the ratio of pressures

$$\frac{p_h}{p_c}=1+\frac{\rho_c u_c^2-\rho_h u_h^2}{p_c}=1+\kappa\frac{u_c^2}{c_c^2}-\frac{\rho_c}{p_c}u_c u_h=1+\kappa M_c^2\left(1-\frac{u_h}{u_c}\right). \tag{A.16}$$

Employing Eq. (A.15) results then in

$$\frac{p_h}{p_c}=1-M_c^2(\kappa-1)\frac{\dot{q}}{p_c u_c}+\mathcal{O}(M^4). \tag{A.17}$$

Combining Eqs. (A.5) and (A.11), the ratio of temperatures can be expressed in terms of heat release and cold gas conditions as well:

$$\frac{T_h}{T_c}-1=\frac{\kappa-1}{\kappa}\frac{\dot{q}}{p_c u_c}. \tag{A.18}$$

Now these relations can be linearized for small fluctuations as they appear in acoustics. Beginning with pressure, Eq. (A.17) will be rearranged (neglecting higher order Mach number terms) to

$$p_h=p_c-(\kappa-1)\frac{\dot{q}u_c}{c_c^2}. \tag{A.19}$$

All variables are then split up into mean values and fluctuations (products of fluctuations are neglected):

$$\overline{p_h}+p_h'=\overline{p_c}+p_c'-(\kappa-1)\frac{\overline{\dot{q}}\,\overline{u_c}+\overline{\dot{q}}u_c'+\dot{q}'\overline{u_c}}{\overline{c_c}^2+2\overline{c_c}c_c'}. \tag{A.20}$$

To first order in fluctuating quantities, one writes (using Eq. (A.4))

$$\overline{p_h}+p_h'=\overline{p_c}+p_c'-\frac{(\kappa-1)}{\kappa}\frac{\overline{\rho_c}}{\overline{p_c}}(\overline{\dot{q}}\,\overline{u_c}+\overline{\dot{q}}u_c'+\dot{q}'\overline{u_c}). \tag{A.21}$$

Subtracting the balance equation of mean values leads to

$$p_h'=p_c'-\frac{(\kappa-1)}{\kappa}\frac{\overline{\rho_c}}{\overline{p_c}}(\overline{\dot{q}}u_c'+\dot{q}'\overline{u_c}) \tag{A.22}$$

and incorporating Eq. (A.18) one finally ends up with a relation between fluctuations of pressure on the cold and hot gases side respectively:

$$p_h'=p_c'-\overline{\rho_c}\,\overline{u_c}^2\left(\frac{\overline{T_h}}{\overline{T_c}}-1\right)\left(\frac{u_c'}{\overline{u_c}}+\frac{\dot{q}'}{\overline{\dot{q}}}\right). \tag{A.23}$$

In order to derive the linearized equation for velocity fluctuations, one starts by rearranging Eq. (A.15) to

$$u_h p_c=u_c p_c+\dot{q}\frac{\kappa-1}{\kappa} \tag{A.24}$$

and doing the split up of mean values and fluctuations (neglecting products of fluctuations)

$$\overline{u_h p_c}+\overline{u_h}p_c'+u_h'\overline{p_c}=\overline{u_c p_c}+\overline{u_c}p_c'+u_c'\overline{p_c}+(\overline{\dot{q}}+\dot{q}')\frac{\kappa-1}{\kappa}. \tag{A.25}$$

Again subtracting the mean balance Eq. (A.24) and rearranging results in

$$u'_{\mathrm{h}} = u'_{\mathrm{c}} + \frac{p'_{\mathrm{c}}}{\overline{p_{\mathrm{c}}}}(\overline{u_{\mathrm{c}}} - \overline{u_{\mathrm{h}}}) + \frac{\dot{q}'}{\overline{p_{\mathrm{c}}}}\frac{\kappa - 1}{\kappa}. \tag{A.26}$$

Applying Eq. (A.24) on the mean values in the second term and expanding the third term, one can write

$$u'_{\mathrm{h}} = u'_{\mathrm{c}} + \frac{p'_{\mathrm{c}}}{\overline{p_{\mathrm{c}}}}\left(-\frac{\overline{\dot{q}}}{\overline{p_{\mathrm{c}}}}\frac{\kappa - 1}{\kappa}\right) + \frac{\kappa - 1}{\kappa}\frac{\overline{\dot{q}}}{\overline{p_{\mathrm{c}} u_{\mathrm{c}}}}\overline{u_{\mathrm{c}}}\frac{\dot{q}'}{\overline{\dot{q}}}. \tag{A.27}$$

Rearrangement and application of Eq. (A.18) finally yields

$$u'_{\mathrm{h}} = u'_{\mathrm{c}} + \left(\frac{\overline{T_{\mathrm{h}}}}{\overline{T_{\mathrm{c}}}} - 1\right)\overline{u_{\mathrm{c}}}\left(\frac{\dot{q}'}{\overline{\dot{q}}} - \frac{p'_{\mathrm{c}}}{\overline{p_{\mathrm{c}}}}\right). \tag{A.28}$$

Appendix B. Linearization of the heat release

Combining constant terms, Eq. (11) can be simplified to

$$\dot{q} = C_2\left(\lambda + 2\sqrt{C_1 u_{\mathrm{c}}}\right) \quad \text{with} \quad u_{\mathrm{c}} \geqslant 0. \tag{B.1}$$

Partial differentiation for u_{c} and multiplication with $u'_{\mathrm{c}}(t-\tau)$ gives the fluctuation of $\dot{q}$ (at time t)

$$\dot{q}' = C_2\sqrt{C_1}\frac{u'_{\mathrm{c}}(t-\tau)}{\sqrt{\overline{u_{\mathrm{c}}}}}. \tag{B.2}$$

For harmonic fluctuations, $u'_{\mathrm{c}}(t-\tau)$ can be expressed as $u'_{\mathrm{c}}\mathrm{e}^{-\mathrm{i}\omega\tau}$, thus the normalized linearized heat release finally becomes

$$\frac{\dot{q}'}{\overline{\dot{q}}} = \frac{u'_{\mathrm{c}}\mathrm{e}^{-\mathrm{i}\omega\tau}}{\lambda\sqrt{\frac{\overline{u_{\mathrm{c}}}}{C_1}} + 2\overline{u_{\mathrm{c}}}}. \tag{B.3}$$

Application of Eq. (B.3) to Eqs. (A.23) and (A.28), replacement of p' and u' by Riemann invariants f and g and rearrangement results in the acoustic transfer matrix (18) for the heat release.

Appendix C. Semi-analytical test case

In this section, semi-analytical results for a simplified model of a Rijke tube are presented in order to illustrate that frequencies and growth rates of eigenmodes can indeed be deduced from a Nyquist diagram, even for strong interaction between acoustic and heat release fluctuations with large interaction index n. Similar treatments are found in [21,45,57].

Consider a generalized Rijke tube of lenght l with a compact heat source located at position $x_{\mathrm{h}} = l/3$ as shown in Fig. 7. A non-ideal acoustic reflection coefficient $r = -0.95$ at the two ends $x = 0$ and $x = l$ is introduced in order to reduce the growth rates of unstable modes, which otherwise tend to be unreasonably large. For simplicity, but without essential loss of generality, the case of vanishing Mach number, $M = 0$, and equal specific impedances at both sides of the heat source, $\xi = \varrho_{\mathrm{h}} c_{\mathrm{h}}/\varrho_{\mathrm{c}} c_{\mathrm{c}} = 1$, is considered. Then the coupling relations for the characteristic wave amplitudes f, g across the heat source simplify considerably. In agreement with (18) and (19) one obtains for fluctuations of pressure and velocity, respectively:

$$f_3 + g_3 = f_2 + g_2, \tag{C.1}$$

$$f_3 - g_3 = (1 + n\mathrm{e}^{-\mathrm{i}\omega\tau})(f_2 - g_2). \tag{C.2}$$

The interaction index n is not set to $\theta(2 + \lambda/\sqrt{C_1 u_{\mathrm{c}}})^{-1}$, as Eq. (19) would suggest, but is treated as an adjustable parameter in this sub-section. The coupling relations across the upstream and downstream ducts are employed as described above, see Eq. (13).

This simple model is most conveniently analysed in non-dimensional variables, with the propagation time for acoustic waves l/c as the characteristic time scale of the problem. The eigenfrequencies ω_n of this system can be computed as solutions to the following dispersion relation:

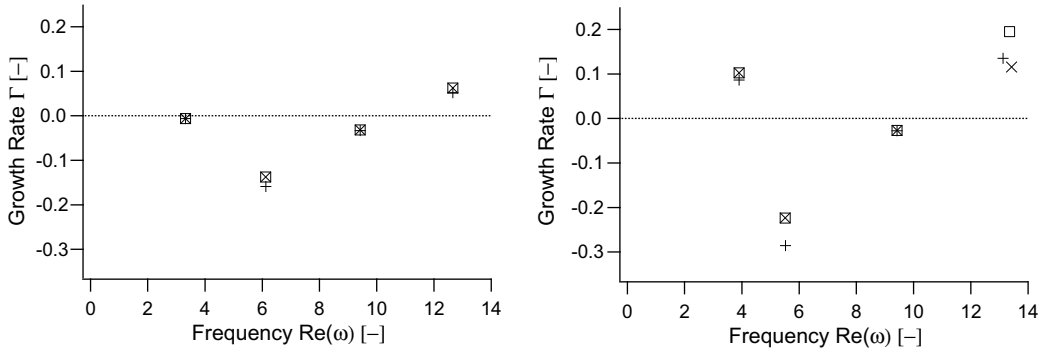

Fig. C.1. Frequeny Re(ω) and growth rate Γ of the first four eigenmodes for interaction indices $n = 0.5$ (left) and $n = 5$ (right). Solution of dispersion relation (□), geometrical interpretation of Nyquist plot (+), iterative solution of $P_{G,m}(\omega_n^*) = -1$ based on fourth order polynomial interpolation of the OLTF (×). Time lag $\tau = 0.1$ and end reflection factors $r = -0.95$.

$$\left(e^{2i\omega} - r^2\right) + \frac{1}{2} n e^{-i\omega\tau}\left(e^{i\omega} + r e^{2i\omega/3} - r e^{4i\omega/3} - r^2\right) = 0. \tag{C.3}$$

Without a fluctuating heat source ($n = 0$), and for open end reflection factors $r = -1$, the eigenfrequencies $\omega_n = \pi, 2\pi, 3\pi, \ldots$ corresponding to "organ pipe modes" are the obvious solutions to this equation. For time lag $\tau = 0.1$, and interaction index $n = 0.5$ and $n = 5$, respectively, the frequencies and growth rates of the first four eigenmodes are shown in Fig. C.1.

Now it is described how the eigenfrequencies can be determined from the open-loop transfer function $G(\omega)$. For the simplified model considered in this section, the OLTF can be formulated in closed form. If the "cut" of the model is placed at position $x_c = 2l/3$, one obtains

$$G(\omega) = -r^2 e^{-2i\omega} \frac{1 + \frac{n}{2}(1 - r^{-1} e^{2i\omega/3}) e^{-i\omega\tau}}{1 + \frac{n}{2}(1 - r e^{-2i\omega/3}) e^{-i\omega\tau}}. \tag{C.4}$$

The Nyquist plots generated with this expression are shown in Fig. C.2, again for the two cases $n = 0.5$ and $n = 5$, respectively, and $r = -0.95$ at the duct terminations. Note that the OLTF-curve starts at the critical point -1 for frequency $\omega = 0$ and then circles the origin in the clockwise direction.

Frequencies $\omega_n^+ \in \mathbb{R}$, for which the distance from the OLTF-curve and the critical point -1 reaches a local minimum, can be identified by inspection of the Nyquist plot, followed by numerical minimization of $|G(\omega) + 1|$. Then the scaling factor σ of the OLTF-mapping in the vicinity of a frequency ω_n^+ is determined as

$$\sigma_n = \left| \lim_{\Delta\omega \to 0} \frac{G(\omega_n^+ + \Delta\omega/2) - G(\omega_n^+ - \Delta\omega/2)}{\Delta\omega} \right|. \tag{C.5}$$

The growth rate of the nth eigenmode is finally computed as the scaled distance of the OLTF-curve from the critical point -1:

$$\Gamma_n = \left\{ -2\pi \frac{|G(\omega_n^+) + 1|}{\sigma \omega_n^+} \right\} - 1. \tag{C.6}$$

The frequencies and growth rates of the first four eigenmodes obtained by this method are also shown in Fig. C.1. Obviously, the agreement with the solutions of the dispersion relation C.3 is very good for small absolute values of the growth rate, i.e. when the system is close to neutral stability, and the OLTF curve passes close to the critical point -1. But even for relatively large absolute values of $|\Gamma| > 0.1$, which correspond to a 10% growth or decay of oscillation amplitude per cycle, the agreement for the frequency of the eigenmodes is very good, while it is acceptable for the growth rate.

In Section 2.3 a second method for determining the frequency and growth rate of an eigenmode from the OLTF has been described. This method is based on a polynomial fit $P_{G,m}(\omega)$ of the OLTF based on a number of discrete collocation points in the vicinity of a frequency ω_n^+. An approximate eigenfrequency ω_n^* is then determined by solving iteratively for $P_{G,m}(\omega_n^*) = -1$. The precise value of ω_n^* will depend on the frequency spacing $\Delta\omega$ of the collocation points, and on the order m of the interpolating polynomial.

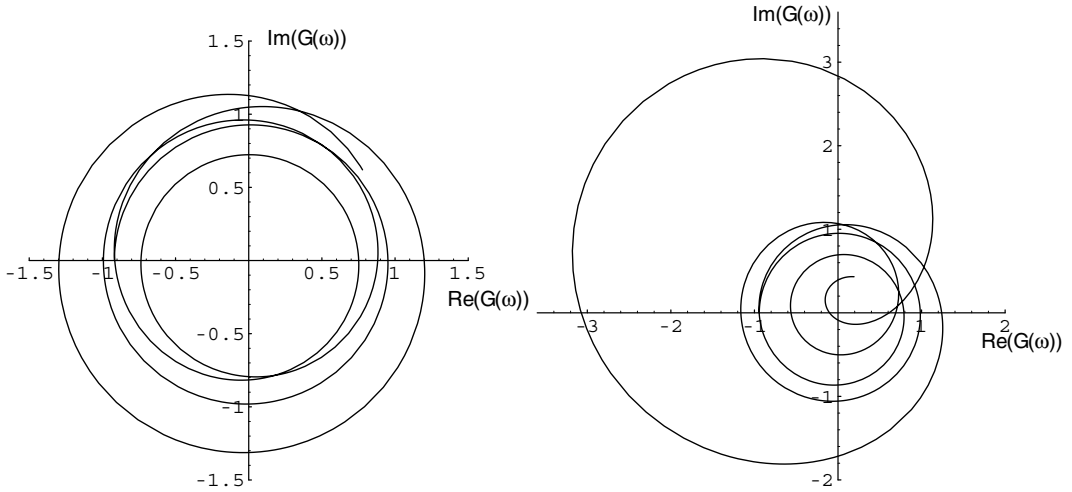

Fig. C.2. Nyquist plot for frequencies $\omega = 0 \rightarrow 14$, indicating the stability of the first four eigenmodes for interaction index $n = 0.5$ (left) and $n = 5$ (right) and time lag $\tau = 0.1$.

In this study, results obtained by this approach from the expression (C.4) for the OLTF with values $\Delta\omega = 0.5, 0.1, 0.02$ and $m = 2, 3, 4$ were compared against each other and against the eigenfrequencies ω_n obtained from the geometrical interpretation of the Nyquist curve. With a frequency spacing $\Delta\omega = 0.5$, one cycle of the Nyquist curve is spanned by less than ten collocation points, which corresponds roughly to the "large frequency spacing" in Fig. 9. Even with such a coarse frequency resolution, the relative difference for the eigenfrequencies was less than 1%, while the relative difference for the growth rate was as much as 50% for a second order polynomial and maximum 10% for a 4th order polynomial. With smaller frequency spacings $\Delta\omega = 0.1$, or $\Delta\omega = 0.02$, the relative difference was less than 1% for both the frequencies and the growth rates, no matter which order polynomial was used.

For analysis of CFD results with a Nyquist diagram presented in the main body of the paper, a frequency spacing of 10 Hz (corresponding roughly to a non-dimensional value $\Delta\omega = 0.1$) and fourth order polynomials were used. The eigenfrequencies ω_n^* obtained for the present semi-analytical case with settings $\Delta\omega = 0.1$ and $m = 4$ are shown in Fig. C.1 The results indicate that the results presented in Section 6 would not change significantly by further decreasing the frequency spacing, or by increasing the order of the interpolating polynomial.

Table D.1
Comparison of frequencies and growth rates determined by the CNN method and a network model, respectively, for the case with an acoustically open end on the upstream side

Mode	Network model		CNN	
	Frequency f_{nw}	Growth rate Γ (%)	Frequency f	Growth rate Γ (%)
1	271.1 − 1.67i	3.94	271.5 − 1.83i	4.32
2	543.1 + 5.75i	−6.43	543.5 + 5.57i	−6.24
3	811.0 − 7.54i	6.01	811.4 − 7.81i	6.24
4	1086.9 + 5.24i	−2.98	1087.9 + 3.23i	−1.85
5	1356.8 + 2.09i	−0.96	1357.0 + 2.38i	−1.10
6	1618.4 − 9.20i	3.63	1618.0 − 12.25i	4.87
7	1913.4 + 13.94i	−4.47	1912.9 + 11.61i	−3.74
8	2152.4 − 10.84i	3.21	2152.5 − 11.27i	3.34
9	2447.8 + 3.07i	−0.78	2442.4 − 0.71i	0.18
10	2719.4 + 1.82i	−0.42	2720.4 + 1.86i	−0.43
11	2960.8 − 0.44i	0.09	2955.2 − 0.69i	0.15

A concluding comment: from a practical point of view, the exact magnitude of the growth rate is not very important if the absolute value of the growth rate of an eigenmode is very large. In that case, the corresponding mode is either strongly damped and not important for overall system behavior, or the mode grows very strongly, indicating that the system design needs to be significantly modified in order to become stable.

Appendix D. Tables of calculated frequencies

See Tables D.1 and D.2.

Table D.2
Comparison of frequencies and growth rates determined by the CNN method and a network model, respectively, for the case with a closed end on the upstream side

Mode	Network model		CNN	
	Frequency f_{nw}	Growth rate Γ (%)	Frequency f	Growth rate Γ (%)
1	97.0 + 0.84i	−5.27	97.0 + 0.83i	−5.23
2	291.4 − 1.73i	3.81	291.7 − 1.85i	4.06
3	486.1 + 1.97i	−2.52	486.1 + 1.98i	−2.53
4	678.0 − 0.47i	0.44	680.7 − 1.11i	1.03
5	873.8 − 1.83i	1.32	873.8 − 1.75i	1.26
6	1071.0 + 5.21i	−3.01	1071.7 + 3.93i	−2.27
7	1258.7 − 7.56i	3.85	1258.8 − 7.94i	4.04
8	1463.9 + 9.50i	−4.00	1464.2 + 8.29i	−3.49
9	1644.1 − 8.86i	3.45	1643.8 − 10.43i	4.07
10	1853.2 + 6.51i	−2.18	1853.4 + 6.27i	−2.11
11	2036.3 − 3.02i	0.93	2034.6 − 6.28i	1.96
12	2233.4 − 0.66i	0.19	2234.1 − 0.30i	0.09
13	2437.4 + 3.66i	−0.94	2433.4 + 5.78i	−0.15
14	2609.2 − 3.81i	0.92	2609.5 − 3.69i	0.89
15	2836.7 + 2.36i	−0.52	2832.8 + 1.45i	−0.32
16	2992.5 − 0.02i	0.00	2990.3 + 0.09i	−0.02

References

[1] P.L. Rijke, Notiz über eine neue Art die in einer an beiden Enden offenen Röhre enthaltene Luft in Schwingungen zu versetzen, Ann. Phys. 79 (1859) 339–343.
[2] J.W.S. Rayleigh, The explanation of certain acoustical phenomena, Nature 18 (1878) 319–321.
[3] G.W. Swift, What is thermoacoustics? A brief description, with technical details and citations, Technical Report LA-UR 04-2298, Condensed Matter and Thermal Physics Group, Los Alamos National Laboratory, Los Alamos, New Mexico 87545 (April 28, 2004).
[4] H.J. Merk, An analysis of unstable combustion of premixed gases, in: 6th Symposium (Int.) on Comb, 1956, pp. 500–512.
[5] A.A. Putnam, Combustion Driven Oscillations in Industry, Elsevier, New York, 1971.
[6] J.J. Keller, Thermoacoustic oscillations in combustion chambers of gas turbines, AIAA J. 33 (12) (1995) 2280–2287.
[7] A.P. Dowling, The calculation of thermoacoustic oscillation, J. Sound Vibration 180 (1995) 557–581.
[8] W. Polifke, Combustion instabilities, Advances in Aeroacoustics and Applications, Von Karman Institute, Brussels, BE, 2004, VKI LS 2004-05.
[9] T. Poinsot, D. Veynante, Theoretical and Numerical Combustion, second ed., Edwards, R.T. Inc., 2005.
[10] T. Lieuwen, V. Yang (Eds.), Combustion Instabilities in Gas Turbine Engines: Operational Experience, Fundamental Mechanisms, and Modeling, no. ISBN 156347669X in Progress in Astronautics and Aeronautics, AIAA, 2006.
[11] C. Hantschk, D. Vortmeyer, Numerical simulation of self-excited thermoacoustic instabilities in a Rijke tube, J. Sound Vibration 277 (3) (1999) 511–522.
[12] T. Murota, M. Ohtsuka, Large-eddy simulation of combustion oscillation in premixed combustor, International Gas Turbine and Aeroengine Congress & Exposition ASME 99-GT-274.
[13] C. Wall, Numerical Methods for Large Eddy Simulation of Acoustic Combustion Instabilities, Ph.D. Thesis, Stanford University, 2005.

[14] T. Poinsot, S.K. Lele, Boundary conditions for direct simulation of compressible viscous flows, J. Comput. Phys. (101) (1) (1992) 104–129.
[15] W. Polifke, C. Wall, P. Moin, Partially reflecting and non-reflecting boundary conditions for simulation of compressible viscous flow, J. Comput. Phys. 213 (1) (2006) 437–449.
[16] D. Bohn, E. Deuker, An acoustical model to predict combustion driven oscillations, 20th International Congress on Combustion Engines, no. G20, CIMAC, London, UK, 1993.
[17] A.P. Dowling, Thermoacoustic instability, in: 6th International Congress on Sound and Vibration, Copenhagen, Denmark, 1999, pp. 3277–3292.
[18] W. Polifke, C.O. Paschereit, K. Döbbeling, Constructive and destructive interference of acoustic and entropy waves in a premixed combustor with a choked exit, Int. J. Acoust. Vibration 6 (3) (2001) 135–146.
[19] C. Pankiewitz, T. Sattelmayer, Time domain simulation of combustion instabilities in annular combustors, Trans. ASME J. Eng. Gas Turbines Power (125) (2003) 677–685.
[20] L. Benoit, F. Nicoud, Numerical assessment of thermo-acoustic instabilities in gas turbines, Int. J. Numer. Methods Fluids 47 (2005) 849–855.
[21] F. Nicoud, L. Benoit, C. Sensiau, T. Poinsot, Acoustic modes in combustors with complex impedances and multidimensional active flames, AIAA J. 45 (2) (2007) 426–441.
[22] W. Krebs, G. Walz, S. Hoffmann, Thermoacoustic analysis of annular combustor, in: 5th AIAA Aeroacoustics Conference, no. AIAA 99-1971, Seattle, WA, 1999.
[23] B. Schuermans, Modeling and Control of Thermoacoustic Instabilities, PhD Thesis, École Polytechnique Fédérale de Lausanne, 2003.
[24] N.A.S. Deo, F.E.C. Culick, Reduced-order modeling and dynamics of nonlinear acoustic waves in a combustion chamber, Combust. Sci. Tech. 177 (2) (2005) 221–248.
[25] K. Truffin, T. Poinsot, Comparison and extension of methods for acoustic identification of burners, Combust. Flame 142 (4) (2005) 388–400, <http://www.sciencedirect.com/science/article/B6V2B-4G7DYRS-1/2/80fee044fb69898a2dba54f4cd4880ae>.
[26] K. Kunze, C. Hirsch, T. Sattelmayer, Transfer function measurements on a swirl stabilised premix burner in an annular combustion chamber, in: International Gas Turbine and Aeroengine Congress & Exposition, no. ASME GT-2004-54106, Vienna, Austria, 2004.
[27] A. Giauque, L. Selle, L. Gicquel, T. Poinsot, H. Buechner, P. Kaufmann, W. Krebs, System identification of a large-scale swirled partially premixed combustor using LES and measurements, J. Turbulence 6 (2007) 1–21.
[28] M. Zhu, A.P. Dowling, K.N.C. Bray, Transfer function calculations for aeroengine combustion oscillations, J. Eng. Gas Turbines Power 127 (1) (2005) 18–26.
[29] W. Polifke, C.O. Paschereit, Determination of thermo-acoustic transfer matrices by experiment and computational fluid dynamics, ERCOFTAC Bulletin 38.
[30] B.B.H. Schuermans, W. Polifke, C.O. Paschereit, Modeling transfer matrices of premixed flames and comparison with experimental result, in: International Gas Turbine and Aeroengine Congress & Exposition, no. ASME 99-GT-132, Indianapolis, Indiana, USA, 1999.
[31] C.O. Paschereit, B.B.H. Schuermans, W. Polifke, O. Mattson, Measurement of transfer matrices and source terms of premixed flames, J. Eng. Gas Turbines Power 124 (2) (2002) 239–247 (originally published as ASME 99-GT-133).
[32] B. Schuermans, F. Bellucci, V. Guethe, F. Meili, P. Flohr, C.O. Paschereit, A detailed analysis of thermoacoustic interaction mechanisms in a turbulent premixed flame, in: International Gas Turbine and Aeroengine Congress & Exposition, no. ASME GT2004-53831, Atlanta, GA, USA, 2004.
[33] A. Huber, W. Polifke, Impact of fuel supply impedance on combustion stability of gas turbines, in: International Gas Turbine and Aeroengine Congress & Exposition, no. ASME GT2008-51193, Berlin, 2008.
[34] T. Schuller, D. Durox, S. Candel, A unified model for the prediction of laminar flame transfer functions: Comparisons between conical and V-flame dynamics, Combust. Flame 134 (1 and 2) (2003) 21–34.
[35] C.O. Paschereit, W. Polifke, Investigation of the thermo-acoustic characteristics of a lean premixed gas turbine burner, in: International Gas Turbine and Aeroengine Congress & Exposition, no. ASME 98-GT-582, Stockholm, Sweden, 1998.
[36] W. Polifke, A. Poncet, C.O. Paschereit, K. Döbbeling, Reconstruction of acoustic transfer matrices by instationary computational fluid dynamics, J. Sound Vibration 245 (3) (2001) 483–510.
[37] A. Giauque, Fonctions de transfert de flamme et energies des perturbations dans les ecoulements reactifs, Ph.D. Thesis, L'Institut National Polytechnique de Toulouse, Toulouse, France, 2007.
[38] T. Lieuwen, Modeling premixed combustion – acoustic wave interactions: a review, J. Prop. Power 19 (5) (2003) 765–781.
[39] C.J. Lawn, W. Polifke, A model for the thermo-acoustic response of a premixed swirl burner: Part II: The flame response, Comb. Sci. Tech. 176 (8) (2004) 1359–1390.
[40] E.G. Neumann, An impedance condition for avoiding acoustic oscillations generated by gas flames, Acoustica 30 (1974) 230–235.
[41] O.L.R. Jacobs, Introduction to Control Theory, Oxford University Press, 1993.
[42] W. Polifke, C.O. Paschereit, T. Sattelmayer, A universally applicable stability criterion for complex thermoacoustic systems, in: 18. Deutsch-Niederländischer Flammentag, VDI Bericht, no. 1313, Delft, NL, 1997, pp. 455–460.
[43] T. Sattelmayer, W. Polifke, Assessment of methods for the computation of the linear stability of combustors, Combust. Sci. Techn. 175 (3) (2003) 453–476.
[44] T. Sattelmayer, W. Polifke, A novel method for the computation of the linear stability of combustors, Combust. Sci. Tech. 175 (3) (2003) 477–498.
[45] K.R. McManus, T. Poinsot, S.M. Candel, A review of active control of combustion instabilities, Prog. Energy Combust. Sci. 19 (1993) 1–29.

[46] M.A. Heckl, Non-linear acoustic effects in the rijke tube, Acustica 72 (1990) 63–71.
[47] K. Jänich, Analysis für Physiker und Ingenieure, Springer, Verlag, Berlin, Heidelberg, New York, 1983.
[48] K.H. Lundberg, Barkhausen stability criterion. <http://web.mit.edu/klund/www/weblatex/node4.html> (2002).URL: <http://web.mit.edu/klund/www/weblatex/node4.html>.
[49] M. Åbom, H. Bodén, Modelling of fluid machines as sources of sound in duct and pipe systems, Acta Acoust. 3 (6) (1995) 549–560.
[50] W. Polifke, A.M.G. Gentemann, Order and realizability of impulse response filters for accurate identification of acoustic multi-ports from transient CFD, Int. J. Acoust. Vibration 9 (3) (2004) 139–148.
[51] S.R. Stow, A.P. Dowling, Low-order modelling of thermoacoustic limit cycles, in: International Gas Turbine and Aeroengine Congress & Exposition, no. ASME GT2004-54245, Vienna, Austria, 2004.
[52] G. Bisio, G. Rubatto, Sondhauss and Rijke oscillations – thermodynamic analysis, possible applications and analogies, Energy 24 (1999) 117–131.
[53] K.I. Matveev, Energy consideration of the nonlinear effects in a rijke tube, J. Fluids Struct. 18 (6) (2003) 783–794.
[54] L. King, On the convection of heat from small cylinders in a stream of fluid: determination of the convection constants of small platinum wires with applications to hot-wire anemometry, Philos. Trans. Roy. Soc. A214 (1914) 373–432.
[55] M. Lighthill, The response of laminar skin friction and heat transfer to fluctuations in the stream velocity, Proc. Roy. Soc. A 224 (1954) 1–23.
[56] B.T. Chu, On the generation of pressure waves at a plane flame front, in: 4th Symposium (International) on Combustion, 1953, pp. 603–612.
[57] A. Kaufmann, F. Nicoud, T. Poinsot, Flow forcing techniques for numerical simulation of combustion instabilities, Combin. Flame 131 (4) (2002) 371–385.